Proceedings World Geothermal Congress 2023
Beijing, China, April 17 – 21, 2023

Exploration History and Conceptual Model of the Dixie Meadows Geothermal Field, Nevada, USA

B. Delwiche[1], R. Libbey[1], M. Folsom[1], A. Johnson[1], J. Murphy[1]

[1]Ormat Technologies Inc.

6140 Plumas St. Reno, NV USA 89519

bdelwiche@ormat.com

Keywords: Geothermal Exploration, Geology, Geochemistry, Geophysics, Nevada, Dixie Meadows

ABSTRACT

Ormat has executed a comprehensive exploration program at Dixie Meadows, Nevada, leading to the discovery of a high permeability, 150°C+ geothermal resource. The reservoir is a low TDS (0.17 wt%) neutral-pH Na-Cl, low NCG fluid of meteoric origin, hosted within Triassic metasediments and Cretaceous intrusive rock. Exploration drilling during the early 1980's and by Ormat in 2012 identified outflow ranging in temperature from 70-140°C that is laterally channeled in the upper 50 m of the subsurface. This outflow is located near the trace of ENE-striking fault zones within permeable units in the alluvium and is also manifested as weak steam vents along the Dixie Valley range front fault scarp which ruptured in 1954 (M6.8). The thermal fluids discharge as hot springs in marshlands to the east.

The initial exploration drilling during the 1980's and during the earliest exploration drilling by Ormat in 2011 failed to identify the source of upflow. A revised conceptual model was developed by Ormat based on detailed geologic mapping and synthesis with the available drilling, geophysical, and geochemical datasets. A deep core hole tested two competing conceptual models and proved the reservoir to be sourced from below the Dixie Valley Fault zone which bounds the eastern front of the Stillwater Mountains. Upflow for the resource is dominantly controlled by a series of ENE-striking faults that contain dilated fractures oriented ENE to ESE that occur at an extensional left step/bend of the Dixie Valley Fault. This paper serves as a case study to document the geoscientific data, conceptual model, and exploration strategy of an archetypal Basin and Range system in Nevada.

1. INTRODUCTION AND EARLY EXPLORATION HISTORY

The Dixie Meadows project is located in west-central Dixie Valley, Churchill County, Nevada, USA near the eastern flank of the Stillwater Mountains. Surface manifestations at the site include weak steam vents that issue along the trace of the ruptured Dixie Valley Fault (DVF; Slemmons, 1957, Caskey et al. 1996, 2004) and approximately 12 to 72°C springs and seeps that occur in a ~5.5 km long NE-SW lineament that emanate from distal segments of the alluvial fans that flank the eastern side of the Stillwater Mountains (Figure 1). The area was designated as a *Known Geothermal Resource Area* (KGRA) by the United States Geological Survey (USGS) in 1974.

Geothermal exploration at Dixie Meadows was originally conducted by the Nufuels Corporation, a division of the Mobil Oil Corporation, during the early 1980s. Nufuels drilled at least 10 shallow to intermediate depth exploration wells (61-446 m depth) near the thermal springs and vicinity of the range front. These exploration efforts delineated a shallow plume of outflowing hot fluid sourcing near the range front and west of the springs with a maximum temperature of 142°C at only 50 m depth (with a pronounced temperature inversion below this). However, the location or structural control on the source of upflow was not identified in this early drilling campaign.

2. REGIONAL GEOLOGY

The Stillwater Range is an uplifted crustal block within the Basin and Range tectonic province and consists of Triassic-Jurassic metasedimentary rocks of marine origin. Early Triassic rocks consist of pelites, quartz arenites, clastic and micritic limestones and late Triassic rocks consist of a thick sequence of pelitic rocks overlain by Triassic-Jurassic calcareous pelites (Nimz et al., 1999). The Triassic units are intruded by Middle Jurassic Humboldt lopolith gabbroic complex and Cretaceous granodiorite and monzonite. Tertiary volcanic and volcaniclastic rocks locally drape non-conformably over all of the Paleozoic and Mesozoic units (Speed, 1976; Oldow, 1984). Early Oligocene andesitic lavas with K-Ar ages of 35 Ma (Riehle et al., 1972) are overlain by an extensive sequence of Oligocene to early Miocene ash-flow tuffs with equivalent K-Ar ages of 32 to 22 Ma (Riehle et al., 1972; Speed, 1976; Burke and McKee, 1979). The ash-flow tuffs are overlain by detrital and fluvial sedimentary rocks capped by Miocene basalts which have K-Ar ages of 13 to 17 Ma (Nosker, 1981).

Within the Stillwater Range, deformed and folded lower Jurassic carbonates, calcarenites, and pelitic rocks overlay Triassic metasedimentary rocks or are in thrust fault contact. The metasedimentary rocks are also in thrust contact with Jurassic intrusive rocks (Speed, 1976). Other structures in the range which extend into Dixie Valley include ENE, N-, NW-, and NE-striking faults. ENE-, NW-, and N-striking faults locally created paleovalleys or canyons in which Oligocene ash-flow tuffs were deposited. The NE-striking faults are broadly parallel to the maximum horizontal stress direction in this region of the Basin and Range and primarily bound the western and eastern flanks of the Stillwater Range and accommodate modern uplift/subsidence.

Dixie Valley is a structural graben complex down dropped along the NE-striking DVF which bounds the eastern flank of the Stillwater Range. The DVF ruptured in 1954 (M_s 6.8) resulting in fault scarps up to 8 m high extending for over 45 km (Slemmons 1957; Caskey et al., 1996). Normal displacements along the eastern margin of Dixie Valley is accommodated by an NE-striking fault system which

borders the western margin of the Clan Alpine Mountains to the east. The graben is filled with thick Quaternary-Tertiary colluvial and alluvial fan deposits, sandy and silty eolian deposits, lacustrine, and playa deposits which reach a cumulative thickness up to 2500 m towards the center of the basin (Iovenitti, 2014a). The alluvial clastic sediments on the basin margins interfinger with lacustrine sediments towards the center of the basin. The basin-fill sediments overly Tertiary volcanic rocks and older Mesozoic intrusive and metasedimentary rocks in the graben.

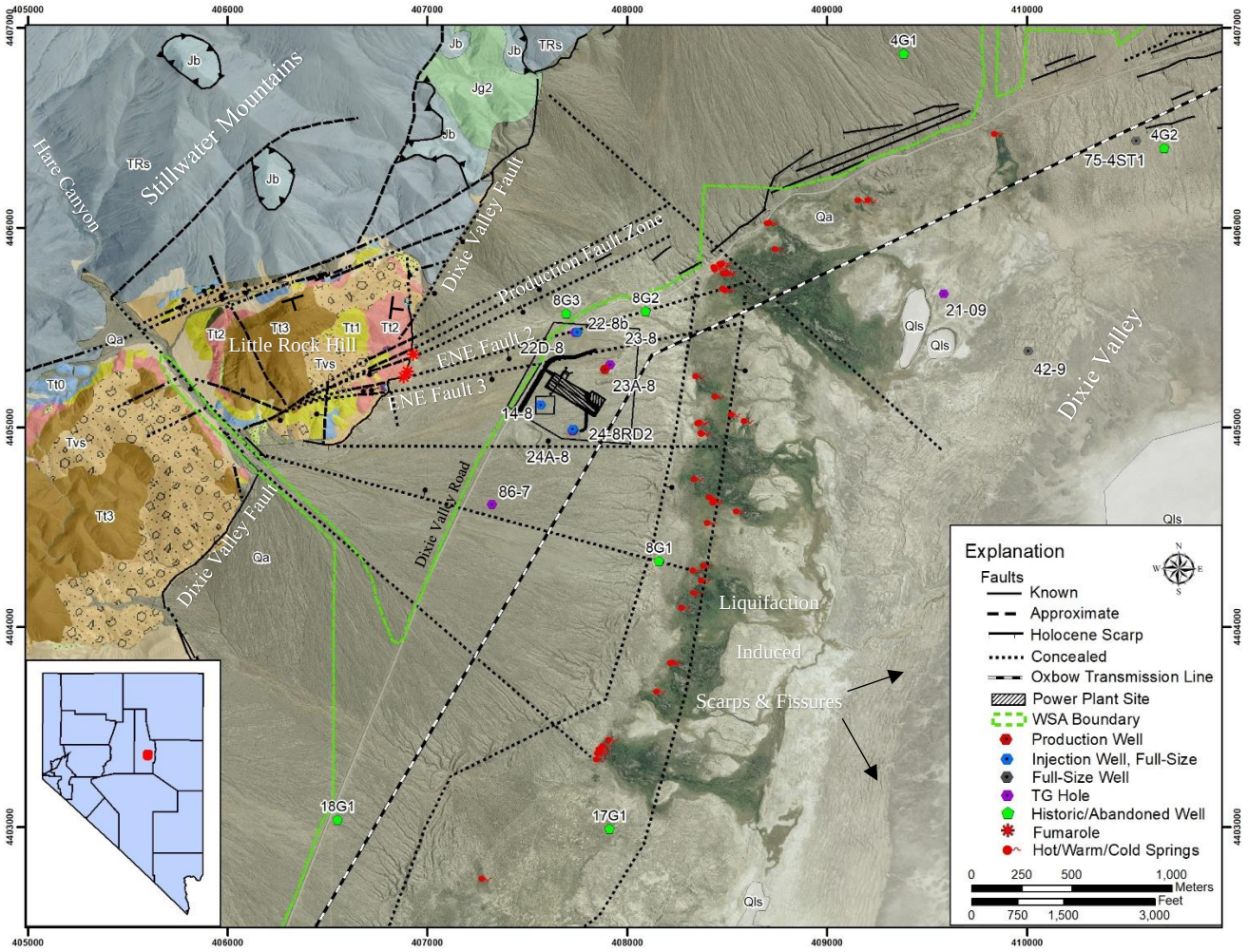

Figure 1: Summary geologic map with wells, general infrastructure, and thermal features. Unit symbols on map Qa: Quaternary Alluvium; Qao: Older Quaternary Alluvium; Qls: Quaternary Lacustrine sediments; Tt3: Tertiary Tuff of Chimney Spring; Tt2: Tertiary Nine Hill Tuff; Tvs: Tertiary volcaniclastic sediment; Tt1: Tertiary Tuff of Dogskin Mountain; Tt0: Tertiary Tuff of Cove Spring; Jb: Jurassic Boyer Ranch Formation; Jg2: Jurassic Gabbro; TRs: Triassic Slate & Siltstone

3. LOCAL GEOLOGY

3.1 Lithology

The youngest lithologic units at Dixie Meadows include alluvial fan and lacustrine deposits which thicken eastward to over >1500 m as controlled by the DVF which dips ~47˚ to the SE and accommodates >2200 m of normal throw (Figure 2). Alluvial fans locally consist of channel, channel bar, and sheet wash deposits containing a mix of cobble- to gravel-size clasts of pre-Tertiary metasedimentary and Tertiary volcanic rocks in sand, silt, and clay matrices. The fans are coarser near the range front containing boulders and grade eastward to finer sediments near the hot springs. East of the springs distal fans containing gravel, sand, silt and clay grade into and interbed with lacustrine mud, clay, and evaporative deposits associated with the Humboldt Salt Marsh.

To the west of Dixie Meadows, four late Oligocene ash-flow tuff units near Hare Canyon comprise the eastern range front and footwall of the DVF Zone (Figure 1). These tuffs are distinguished by their relative abundance and type of phenocrysts including quartz, biotite, plagioclase, and sanidine and are inferred to correlate with dated tuffs which have $^{40}Ar/^{39}Ar$ radiometric ages ranging from 25.07-30.13 Ma (Table 1, Henry et. al, 2004a, C. Henry, personal communication, August 5th, 2013). Cumulatively, the tuffs are about 180 m thick at the range front and are tilted eastward along the DVF by drag folding. Along the northern rim of Little Rock Hill, the tuff deposits dip SE and change from steep to moderate. Here the basal tuff of Cove Spring mantles the Triassic slate and contains abundant lithic clasts, and dips steeply S to SE. The tuffs are interpreted to fill a paleovalley that trends NE- to ENE. Furthermore, the tuffs form a paleovalley margin where they pinch out towards the NW against Triassic basement rocks (Figure 1). At the range front, the tuffs are also locally intruded by aphyric basaltic dikes along ENE-striking fault zones. Within the basin at Dixie Meadows, deep drilling has encountered the same sequence of ash-flow tuff which are >730 m thick beneath Tertiary basalts

which are ~60 m in thickness. The eastward thickening of tuffs indicates a paleodepositional center in Dixie Valley which existed as early as the late Oligocene and prior to uplift of the Stillwater Range (Delwiche, 2011).

Locally Triassic marine metasedimentary rocks of a continental slope depositional environment comprise the eastern slope of the Stillwater Range and include slate, metasiltstone, and localized metalimestone. Additionally, the Jurassic Boyer's Ranch Formation locally consists of metamorphosed continental shelf deposits including metasandstone, metaconglomerate and metalimestone and form allochthonous thrust plates above the Triassic slate and siltstone sequence (Figure 1). The Boyer's Ranch formation, in turn, is intruded by Jurassic gabbro (Speed, 1976, Oldow, 1984). Both Triassic metasedimentary rocks and Jurassic granodiorite have been encountered by deep drilling at Dixie Meadows within the basin and comprise the footwall along the DVF (Figure 1).

Ash-Flow Tuff	Symbol	Thickness	$^{40}Ar/^{39}Ar$ Age	±1σ	Mineral	Total %	Plagioclase		Quartz		Sanidine		Biotite		Other
		meters	Ma				%	mm	%	mm	%	mm	%	mm	
Tuff of Chimney Spring	Tt3	125-354	25.07	0.06	sanidine	25-40	1-4	<0.5-1x1-3	10-20	1-2	10-20	0.5-1x2-3	≤1	<1	
Nine Hill Tuff	Tt2	0-64	25.25	0.06	sanidine	3-6	0-1	1x3	<1	1-2	2-3	0.5-1x3-4	<1	≤1	hornblende, anorthoclase
Tuff of Dogskin Mountain	Tt1	26-95	29.21	0.1	sanidine	20-25	15-20	0.5-1x2-3	tr	1-2	<1	1x2	1-3	0.5-2	
Tuff of Cove Spring	Tt0	25-86	30.36±0.011		sanidine	8-12	1	0.5-2x2-3	<1	≤0.5	7-9	0.5-2x2-3	≤1	<0.5-1.5	

Table 1: Summary of ash-flow tuff units found locally at Dixie Meadows. Age dates taken from Henry, 2004a and C. Henry, personal communication, August 5th, 2013.

3.2 Surface Manifestations, Alteration, and Mineralization

A ~2km long, NNE trending zone of warm and hot springs (max temp ~72°C) issue at an elevation of approximately 1040 masl at the toe of the alluvial fan that drapes the Dixie Meadows project area. The springs issue adjacent to ambient temperature springs, which together create a marshland area in the basin. The highest temperature group of these springs issue at the intersection of the inferred trace of the ENE Production Fault zone with the edge of the alluvial fan. Additionally, several weak steam vents (temperatures up to 90°C) are observed along the DVF scarp near the intersection with the ENE-striking faults, around which salts, native sulfur, and sulfates are actively deposited in trace amounts (Figure 1).

Along the eastern range front and DVF, Tertiary ash-flow tuffs are locally argillically and advanced argillically altered, iron stained, and locally silicified. Hyperspectral data indicate an abundance of kaolinite and montmorillonite clays (Littlefield, 2011 unpublished work). Outcrops of mineralization and alteration are concentrated in the damage zones of several ENE-striking faults and include chalcedonic veins up to ~1cm thick, leaching, silica replacement, and abundant iron staining within tuff formations. The southernmost ENE-striking fault #3 at Dixie Meadows is of a different mineral character and contains abundant gypsum accompanied by leaching, clays, and iron staining.

Above the DVF and along the eastern face of Little Rock Hill, is a massive deposit of calcite and silica 0.5-1 m in thickness distributed over an area ~160 m^2 (Figure 1). Bladed calcite and chalcedony replacements of calcite with bladed textures are indicative of paleo boiling conditions. These deposits are brecciated, slicked and corrugated reflecting a long history of fault reactivation, mechanical deformation, thermal fluid circulation, and mineral precipitation.

3.3 Structure

The older fault zones in the area include thrust faults that juxtapose the Jurassic Boyer Ranch formation or Jurassic granodiorite above Triassic metasedimentary sequences. These fault zones are a few meters to 20 meters thick consisting of breccia, slicked material and commonly calcite veins. The thrust faults are considered remnant features which likely do not contribute to the local reservoir permeability.

The DVF zone, located west of Dixie Meadows, is a complex system of subparallel moderate and steeply dipping normal faults generally striking NE along the eastern flank of the Stillwater Range and western part of Dixie Valley which includes the range-bounding fault that accommodates >2000 m of vertical offset based on the depths at which late Oligocene tuffs were intercepted in well 42-9. Local scarps 1 to 4 m in height delineate the trace of the DVF which ruptured in 1954 resulting in a magnitude 6.8 M_S earthquake (Bell and Katzer, 1987; Caskey et al., 1996). The epicenter of the 1954 earthquake was at the mouth of Hare Canyon, directly west of Dixie Meadows (Page, 1965). In addition to young scarps, the DVF surface locally is recorded in a massive calcite-silica deposit and on one outcrop of densely welded upper section of the Nine Hill Tuff. Measurements of slicked surfaces suggests a ~46 to 52°SE dip and intercepts in drill holes suggest a 47°SE dip of the range front fault. This orientation agrees well with fracture orientations picked from downhole acoustic televiewers and electrical imaging tools. Based on gravity datasets, a pediment fault is inferred near the hot springs, which may be mechanically linked with the range front fault to accommodate normal offsets (Figure 10B).

Other local fault sets strike ENE, NW, WNW to EW, and NNE to N (Figure 1). These faults all appear to predate activation of the DVF and possibly developed during different tectonic events. Most faults in the sedimentary basin are concealed so the surface traces are approximated. ENE-striking faults accommodate oblique slip and are the most prominent and accommodate a 2000 m right-step of the Stillwater Mountains ~2.5 km to the northeast of the Dixie Meadows prospect area. The ENE-striking faults are considered possibly the oldest set and formed likely during an earlier tectonic period prior to the late Oligocene. This is evidenced by a very prominent set of ENE-striking joints greater than 50 m in height over a distance of at least 30 m exposed in Hare Canyon within the Triassic sequence. The joint set does not exhibit any brecciation suggesting that the fabric pre-dates deposition of the marine sediments. Also, ENE-striking fault surfaces are coincident with the base of the slope associated with the paleovalley margin located north of Little Rock Hill (Figure 1). Topographic relief on the Triassic basement rocks changes rapidly across the ENE fault which

is down thrown on the south side. The sequence of Tertiary tuffs occupies the associated accommodation space and thin or pinch out northwards towards the margin (Figure 1). This observed relationship indicates that the ENE fault was active prior to the late Oligocene.

Based on drilling data and image logs, the geothermal reservoir at Dixie Meadows associates with one of the ENE-striking fault zones which cuts tuff at the range front in the footwall of the DVF but otherwise has no surface expression within the sedimentary basin that overlies the basement region where the fault is producible (Figures 1 & 2). The damage zone associated with this fault is about 3 m thick in the tuff, but is greater than 100 m thick within the deeper Triassic slate and metasiltstone formations. This relationship indicates that a much longer history of deformation is recorded in the Triassic basement rocks than what is recorded in the tuffs, and therefore the inception of the ENE-striking fault zone must pre-date deposition of the tuffs.

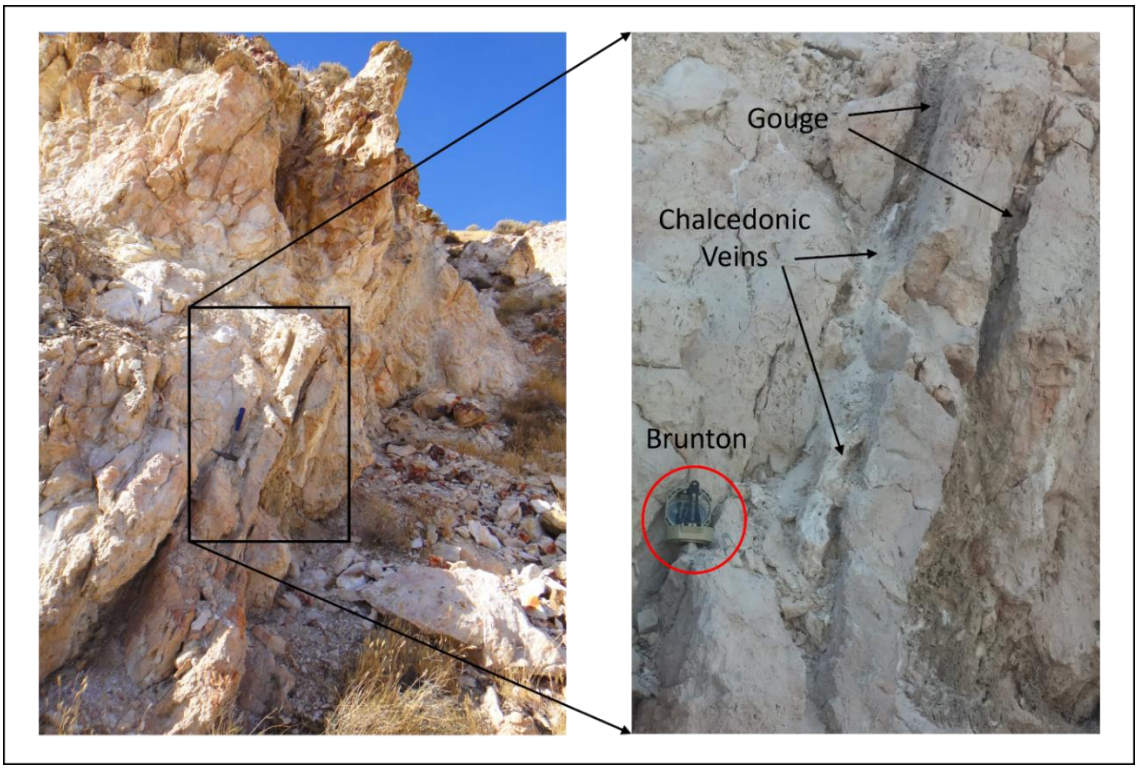

Figure 2: ENE-striking fault damage zone in rhyolitic ash-flow tuff (Tt2, Nine Hill Tuff)

Kinematic indicators measured on fault surfaces and in core samples indicate oblique slip on the producible fault. This suggests that the maximum horizontal principal stress and vertical stress vectors are similar in magnitude, which could explain the enhanced dilation of fractures observed in the fault zone if the magnitude of the minimum horizontal stress is relatively low. Evidence for the eastward continuation of the producible ENE-striking fault includes Holocene scarps 1-3 km ENE of the production well 23A-8 and deep drilling data from 75-4ST1 (Figure 1). However, results from 75-4ST1 have demonstrated that the eastern portion of the fault zone is impermeable at depth, hosts sub-commercial temperatures, and is outside the geothermal reservoir.

Regionally, the maximum horizontal principal stress vector is oriented approximately N35°E, which (in agreement with the Mohr-Coulomb law of failure) favors normal displacements along the DVF that strikes approximately N37°E (Figure 3A; Hickman et. al, 2000; Hammond et. al, 2005; Huang et. al, 2012). However, from drilling data, the DVF is gouge-rich and relatively impermeable and not a direct permeability control of the geothermal reservoir. The ENE-striking faults are not oriented optimally within the current regional ambient tectonic stress field to accommodate displacements. Natural fractures at depth oriented similar to tensile drilling induced fractures are expected to be most relatively dilated and permeable under the local stress field conditions (e.g. Huang et al. 2012). Based on the average orientation of tensile drilling induced fractures from deep drilling at Dixie Meadows, the stress field locally is rotated to approximately N70°E, which can favor displacements along and dilation of ENE-striking fractures (Figures 3b & Figure 4).

WNW- to EW-striking faults exist in the southern part of the field. There is one fault zone expressed at the surface recorded in the ash-flow tuff sequence near Hare Canyon. The other evidence for WNW- and EW-striking faults comes from drilling parameters and image logs from both shallow and deep drill holes including 24A-8, 24-8, and 14-8 which were completed in the sedimentary basin. These faults all dip N to NNW and are conjugate to the ENE-striking production fault. The WNW- and EW-striking faults appear to be mechanically linked with the ENE-striking faults to the north and form a graben which extends approximately orthogonal to the DVF. This E-W graben is inferred to have formed by influence of strain across the active DVF.

Evidence for a NW-striking fault extending from Hare Canyon into the alluvial basin includes the normal offset of tuffs across the canyon and a fault scarp from the 1954 rupture event. The trace of the NW fault is lost upon exiting the mouth of Hare Canyon towards the SE; however, a group of warm springs emanating from the distal portion of the alluvial fans is along trend with the lateral projection of this fault. Based on geophysical data and distribution of temperature data, the NW-striking fault appears to bound the

shallow outflow of the geothermal system on the south. The producible ENE-striking fault also terminates into the NW-striking fault in Hare Canyon providing a western bounds on the possible extent of the geothermal reservoir.

South of Dixie Meadows and west of the dry lakebed, liquefaction-induced scarps and fissures have been documented, including lurch and collapse features up to 1-2 m in depth. A thin veneer of fine sand and silt is present in the liquefaction zones, which is believed to be related to expelled-water phenomena along these features (Bell and Katzer, 1987). The ponds on the east side Dixie Meadows are likely associated with liquefaction that is known to have occurred during the 1954 earthquake, or perhaps earlier tectonic events along the active fault zone (Wesnousky, 2003).

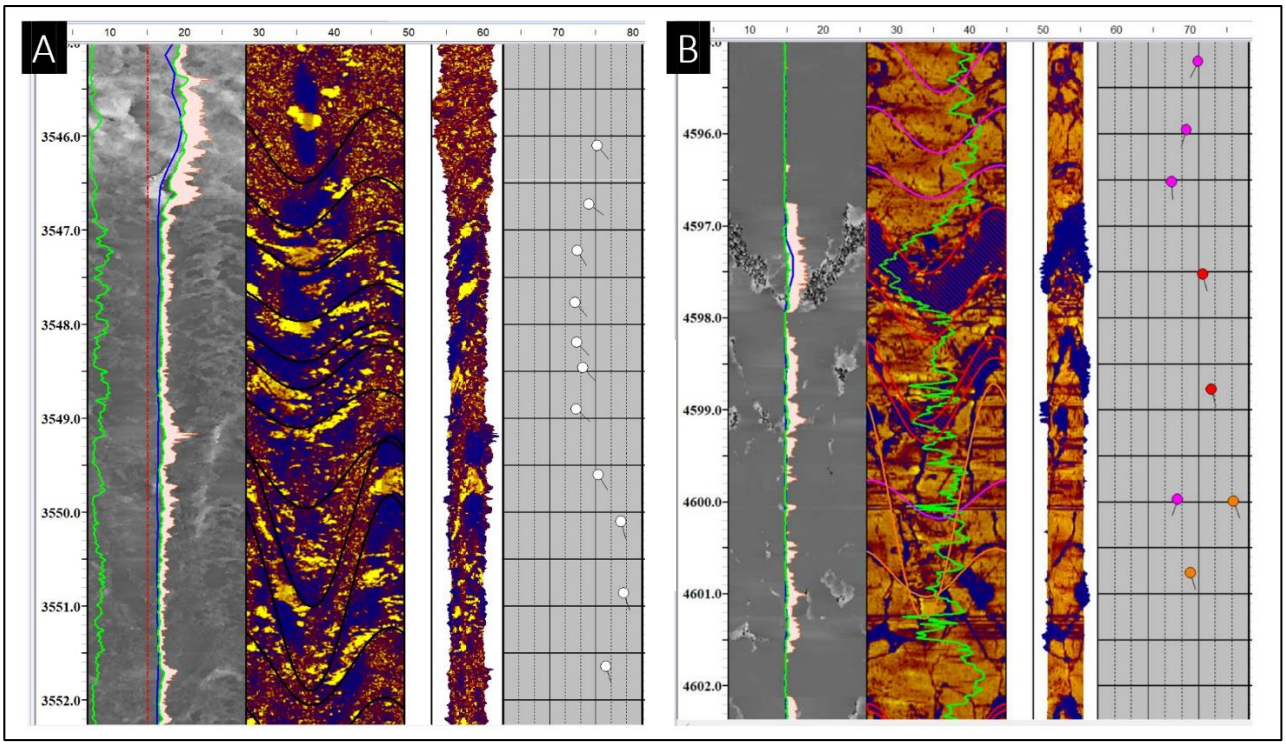

Figure 3: (A) ABI acoustic image of the DVF zone. Sealed fractures (black sinusoids and white tadpoles) dip moderately south east. (B): ABI 40 acoustic image of the producible ENE-striking fault zone. Sealed (pink), partially open (orange), and open fractures (red) represented by colored sinusoids and tadpoles.

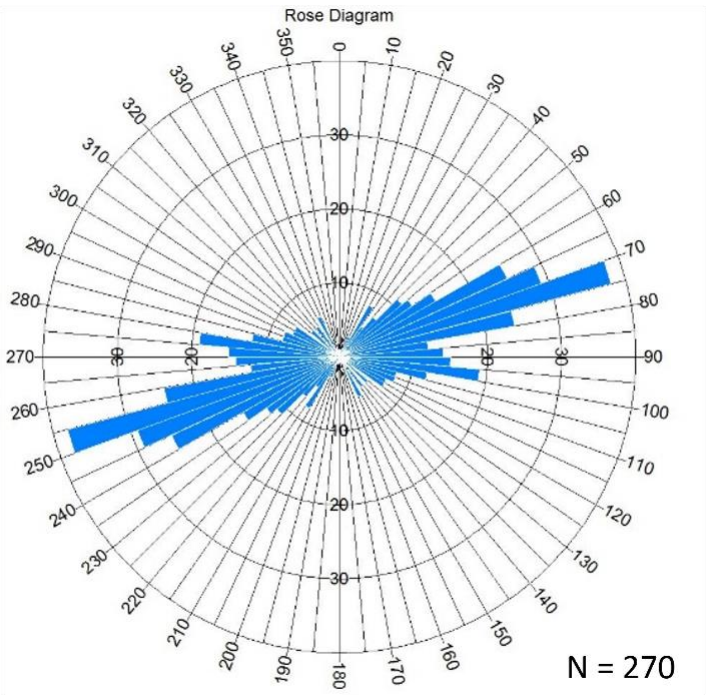

Figure 4: A population distribution of induced tensile fractures from an acoustic image log in exploration core hole 23-8.

4. GEOCHEMISTRY

Well discharge fluids collected from 23A-8 and 22D-8 define a low TDS (850-1030 ppm) Na-Cl reservoir fluid (Figure 5, Table 3) with ~0.1 wt% NCG concentration. SiO2 concentrations of 186 to 215 ppm suggest equilibrium with chalcedony in the reservoir, and that the parent fluid in the deeper (untapped) region of the upflow may reach temperatures as high as 165°C. The low TDS nature of the reservoir fluid is consistent with non-magmatic deep circulation systems hosted in Cl-deficient host rocks (e.g., substrata that has low leachable volumes of volcanic glass or evaporitic salts). Downhole data confirms that the reservoir is hosted in metasediments and crystalline intrusive rocks (gabbros and granodiorite), both which have minimal budgets of leachable Cl.

There is an inverse correlation between warm/hot spring SiO2 and Mg, which suggests mixing of geothermal outflow fluid with a groundwater source. The occurrence of cold springs adjacent to the warm and hot springs that occur in the Dixie Meadows marshlands also supports this mixing hypothesis. The mixing fluid source is expected to be derived from the pronounced highlands that occur directly to the west of the geothermal system, but there may also be mixing with steam condensate from the shallow boiling outflow. The spring chemistry has reduced Na, K, Ca, Cl, HCO3, and SiO2 relative to the reservoir fluid (Table 3). Mg is slightly elevated in the springs relative to the reservoir fluid, but with maximum concentrations of 1.2 ppm these Mg values do not indicate notable mixing with mineralized groundwater, but rather a dilute fluid. SiO2 values for the hot springs do not exceed 110 ppm as a result of the dilution by these mixing waters and some precipitation of silica along the outflow path (Figure 6). Chalcedony geothermometer estimates from the spring fluids of 116°C are thus not illustrative of reservoir equilibrium temperatures. Na-K and Na-K-Ca geothermometers provide estimates of ~140°C, which are closer to the confirmed maximum reservoir temperature of 154°C.

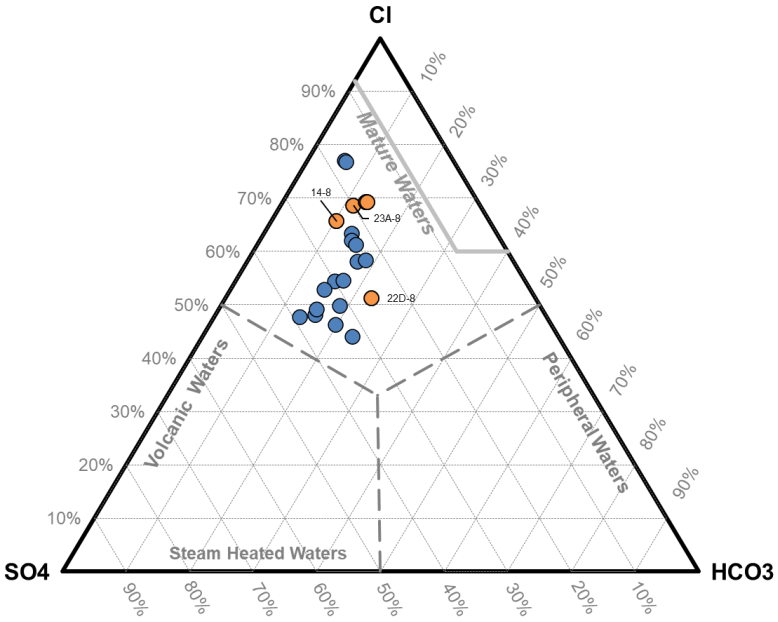

Figure 5: Ternary anion diagram for Dixie Meadows fluid samples.

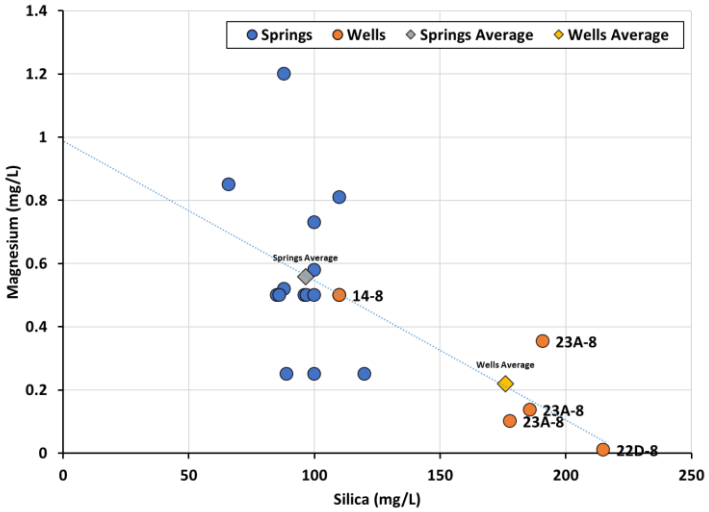

Figure 6: Mg vs SiO2 bivariate plot for Dixie Meadows fluid samples.

Sample	T (°C)	pH	TDS ppm	Na ppm	K ppm	Ca ppm	Li ppm	Mg ppm	Cl ppm	SO4 ppm	HCO3 ppm	F ppm	B ppm	SiO2 ppm
22D-8 Reconstructed Reservoir Chem	154	7.3	821	209	13	5.5	0.4	<0.01	185	93	101	12	0.9	200
Spring 4	70	8.5	591 ⇩	170 ⇩	6 ⇩	3.9 ⇩	0.4	<0.5	150 ⇩	95	56 ⇩	11	0.9	110 ⇩

Table 2: Representative reservoir and hot spring chemistry at Dixie Meadows.

5. DRILLING EXPLORATION HISTORY

5.1 Ormat Exploration 2011 - 2017

The first well drilled by Ormat at Dixie Meadows was 42-9 from 9/20/2011 to 10/26/2011. This was a directional full-size exploration well with 13-3/8" casing to 1134 m (3721 ft) and a 12-1/4" directional open hole to 2268 m (7442 ft). The location was permitted under an EA initiated by Terragen Power Company (TGP), and the well targeted theoretical piedmont faults interpreted from MT and gravity datasets. The well encountered 1524 m (5000 ft) of basin-fill sediments above Tertiary volcanic and volcaniclastic sequences to total depth. No significant fluid losses or fault zones were encountered in this well, and the maximum Horner projection bottom hole temperature was 119°C (Dowdle & Cobb, 1975). The well was secured without testing although was later tested in 2019 and yielded an injectivity index of 0.14 GPM/psi.

Following the drilling of the sub-commercial 42-9 well, during 2011-2012, additional exploration studies were performed including geologic mapping, CSAMT, and a second phase of ground-based gravity. Two temperature gradient TG core holes, 22-8b and 86-7, were drilled to total depths of 305 m . These holes were completed with 4-1/2" HWT surface casing to 52.7 m and 89.3 m, respectively, and 2-3/8" slotted tubing to 305 m TD. The purpose of these holes was to explore for potential unknown faults and to investigate a large magnetic low anomaly within the alluvial fans which extends from the eastern range front near Hare Canyon eastward to the Dixie Meadows Hot Springs. No faults were encountered in either well and fluid losses were also minimal. However, anomalous high shallow temperatures with deeper reversals were observed in both wells with maximum temperatures of 144°C at 52.4 m and 101.6°C at 97.5 m in 22-8b and 86-7, respectively. The reversal in 22-8b also correlated well with a similar reversal observed in the historic 8G3 well, which was drilled at a location 104 m northwest of 22-8b on the northwest of Dixie Valley Road (Figures 1 & 7).

The high shallow temperatures cause the obliteration of magnetic minerals within the alluvial sediments, which has resulted in the observed magnetic low anomaly at Dixie Meadows (discussed further below). At the range front, the coincidence of 1) fumaroles, 2) hydrothermal mineralization, 3) a magnetic low, and 4) the intersection of the DVF with several ENE-striking faults suggest that thermal fluids are upwelling to the shallow subsurface in this vicinity and outflowing laterally east and southeastward within layered alluvial sediments towards the discharge point of the thermal springs in the basin.

Core hole 23-8 was drilled to 4700 ft in 2015 to test the permeability characteristics of the DVF and ENE structures. This well consists of 4-1/2" casing to 829 ft, HQ-size hole (3.89") to 1432.5 m (4700 ft), and 2-3/8" slotted tubing to 1430.1 m (4692 ft). This well encountered a thick sequence of alluvial sediment to 1057.7 m (3470 ft) above the DVF. The DVF, which was crossed between 1054.6 – 1066.8 m (3460 - 3500 ft), exhibited relatively low-grade mineralization including clay, calcite, hematite, chlorite, and minor pyrite. Only minor fluid losses were encountered in the DVF and core samples did not indicate open-space mineral growths. Additionally, as the well was deepened, maximum register thermometers (MRT's) indicated increasing conductive temperatures below the DVF. The well was deepened to intersect an ENE-striking fault near 1402 m (4600 ft) where MRT's reached 150 °C, total loss of circulation occurred, and open fractures were observed in core samples and in the acoustic (ABI-40) image log. Fracture orientations picked from the acoustic image log also confirmed the ENE orientation of open fractures. Subsequent injection testing on 23-8 yielded a low injectivity index attributed to the small hole diameter and mud still in the hole. However, pressure fall-off data indicated a high skin factor (20) indicating near-wellbore blockage surrounded by higher permeability. Well 23-8 was considered a success which located a 154°C geothermal reservoir.

24-8 is a full-sized well that was drilled in 2015-2016 to a depth of 932.7 m (3060 ft) at a location 372 m southwest of 23-8. The goal of 24-8 was to further delineate the reservoir and secure potential injection. This well consists of 13-3/8" casing to 857.4 m (2813 ft) and a 17.5" open hole to 932.7 m (3060 ft). 24-8 was planned to target two additional ENE-striking fault zone south of the ENE-striking fault which 23-8 intersected. The well was drilled entirely within basin-fill sediments above the DVF and a total loss of circulation occurred at 898.9 m (2949 ft). The well was completed blind to 932.7 m (3060 ft) and injection tested. The initial test yielded an injectivity index of 10.7 GPM/psi. The well was considered for a potential injector so the decision was made to sand back and cement casing above this permeable zone and complete the well for additional testing.

Following the success of 24-8, a commercial production well was then planned in order to secure production towards the goal of conducting a long-term test. Well 23A-8 twinned 23-8 and was completed in 2016 to 4758 ft. This well was completed with 16" casing to 2095 ft, a 14-3/4" directional hole to 4758 ft, and a 9-5/8" slotted liner to 1450.2 m (4733 ft). This well encountered 1039.3 m (3410 ft) of basin-fill sediments that were directly juxtaposed against Triassic slate and metasiltstone across the DVF at 1051.6 m (3450 to 3500 ft). Total loss of circulation occurred at 1397 m (4583 ft), and numerous drilling breaks were encountered beyond this, with the last drilling break observed at 1450.2 m (4758 ft). A Schlumberger FMI log was run in the well, which reveal large aperture open fractures (up to 30.5 cm or 12 inches) that strike ENE to WNW and dip SSW. The open fracture populations from 1396 –

1450.2 m (4580 to 4758 ft) are inferred to correlate with an ENE-striking fault defined at the range front in the late Oligocene Nine Hill Tuff exposed in the footwall of the DVF. Flow testing of 23A-8 yielded a maximum flowing temperature of 150.5°C and a productivity index of 142 GPM/psi was calculated.

Before a long-term test could be conducted, additional injection capacity was needed. Additional work was deemed necessary to define additional drilling targets. Core hole 24A-8 was drilled during April, 2016 adjacent to 24-8 with the goal of defining a shallow loss circulation zone encountered in 24-8 near 130.4 m (428 ft). 24A-8 was completed vertically with 4-1/2" HWT casing to (46 m (151 ft), HQ-size hole to 228.6 m (750 ft), and slotted 2-3/8" tubing to total depth. An ABI-43 acoustic tool was logged in the well. Fracture picks from the image log and core samples define an E-W-striking fault zone that dips moderately north. Injection testing of 24A-8 yielded low permeability and a low skin. Additional exploration was deemed necessary to defined suitable injection targets.

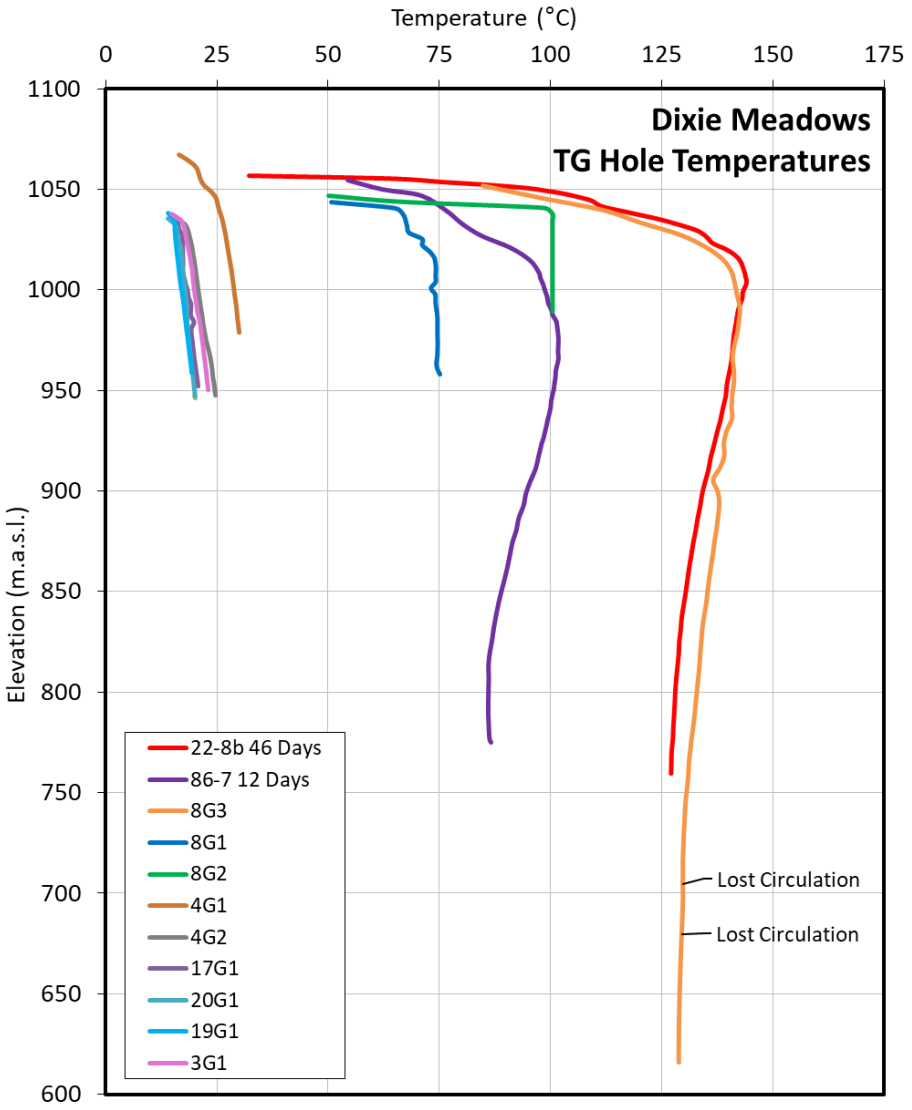

Figure 7: Static temperature profiles of initial exploration holes from Nufuels (1982) and early exploration holes from Ormat (2012).

Further exploration studies were conducted at this time including geologic mapping, density measurements, additional MT acquisition and processing, and gravity modeling. Well 75-4 was sited 2.8 km (1.7 miles) ENE of 23A-8 and was drilled to explore for permeability associated with a series of ENE-striking faults that are defined by fault scarps in alluvial sediments and by geophysics. 75-4 was drilled in 2017 and completed as a forked well. The initial leg was drilled directionally NNW to 1524 m (5000 ft) total depth, and the second leg was achieved with a whipstock and was drilled directionally SSE to 1669.1 m (5476 ft) total depth. The initial leg consists of 13-3/8" casing to 760 m (2493 ft), 12-1/4" hole to 1524 m (5000 ft), and an 8" slotted liner from 730 to 1063.7 m (2395 to 3490 ft). The second leg consists of a whipstock with top at 698.6 m (2292 ft) in milled 13-3/8" casing from 698.6 to 713.5 m (2292 to 2341 ft), a 12-1/4" hole to 1669.1 m (5476 ft) total depth, and a 9-5/8" to 5" slotted liner to 1667.6 m (5471 ft). Both well legs encountered 1097.3 m (3600 ft) of basin-fill sediments above intrusive rocks including Jurassic granodiorite, diorite, and gabbro. The first leg crossed the DVF at 1319.8 m (4330 ft) marked by a change in lithology from granodiorite to gabbro, which in turn, persists to the total depth of the leg. FMI image logs confirmed that both wells encountered numerous ENE-striking fault zones although only minor fluid losses were experienced. The second leg was drilled in the immediate hanging wall of the DVF in attempt to cross open/dilated fractures. A rig test performed after completion yielded injectivity indices ranging from 1.89 to 3.5 GPM/psi. Later static surveys measured a maximum near-equilibrated temperature of 97°C near bottom hole.

Within the drill holes, generally abundant smectite clay and iron oxides are observed at depths <30 m. Below this calcite becomes abundant and forms a dense matrix cement of the alluvial sediments with increasing pyrite and chlorite. Commonly calcite veins are observed which fill fractures within the basin fill sediments. The DVF zone itself encountered near 1000 m depth contains clay, calcite, chlorite, and sericite mineralization. Within the Triassic siltstone and slate formations, ENE-striking fractures commonly are filled by chalcedony and calcite veins. The production zone encountered in 23-8 and 23A-8 near 1400 m depth within slate and siltstone formations contains chalcedonic veins, open space euhedral quartz, pyrite, and open space euhedral natrolite.

5.2 2017 Long-Term Test

Following the completion of 75-4ST1, Ormat performed a 46-day flow and injection test from April 27 to June 11, 2017 (summarized by Akerley et al., 2018). A pump was installed in 23A-8 along with a test apparatus including baker tanks, generators, pumps, and temporary flow lines for injection to 24-8 and 75-4ST1. Downhole pressures were monitored in offset wells. Five spring locations were also monitored for temperature, electrical conductivity (EC), and spring pool stage during the flow and injection testing activities to assess the degree of hydraulic connectivity between the geothermal reservoir and springs at Dixie Meadows (BLM, 2021 Appendix M).

Geothermal brine with a temperature of 150.5°C was pumped from well 23A-8, with discharge rates decreasing over time from approximately 2080 to 1340 GPM due to declining injection capacity, which is discussed later. The average production rate was approximately 1600 GPM (Figure 8**).** The brine flashed in a separator on the 23-8 pad and was gathered in two 24K gallon baker tanks and pumped to wells 24-8 and 75-4ST1. The discharged brine was then reinjected into both wells with assistance from high pressure booster pumps.

Well 24-8 initially injected at a rate of 2500 GPM but as reservoir pressure rose the rate declined to around 1300 GPM (Figure 8), while the injection rate was relatively constant at Well 75-4ST1 at an average of 165 GPM (Figure 8). The average injection rate was approximately 1350 GPM, with the volume lost between production and injection due to evaporative losses from holding tanks and cooling of the fluid.

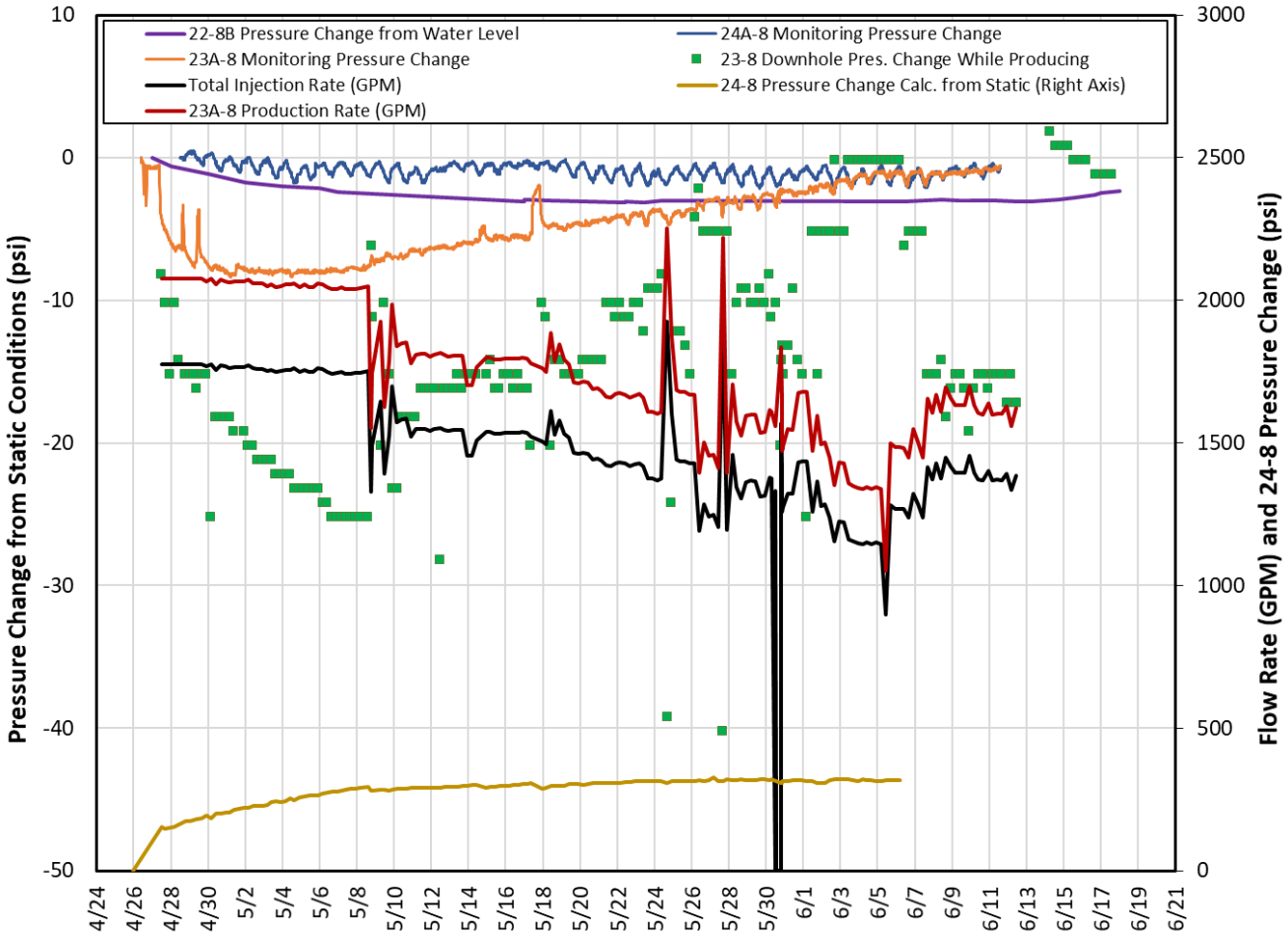

Figure 8: Long-term flow test monitored well parameters

The results of the test indicated that 75-4ST1 exhibited sub-commercial permeability. Well 24-8 exhibited a trend towards stabilized pressures and flow and was deemed a useable injector with moderate permeability. The 23A-8 well demonstrated to be a very permeable producer with no pressure drawdown measured during the test and minimal pressure drawdown with recovery of 8 psi

observed in monitored well 23-8 (Figure 8). With an installed Ormat OPP800 pump, 23A-8 is capable of producing approximately 5500 GPM. Springs monitoring during the flow test exhibited little to no variances in temperature, spring pool height, or EC outside of what appears to be natural variations recorded before and after testing (BLM, 2021 Appendix M).

A reservoir model was also developed in parallel to the long-term test which integrated a 3D geological model, all test data, and was calibrated to match the observed performance of monitored and tested wells. The model was utilized to test reservoir parameter sensitivities of various production and injection scenarios.

Following the results of this test and reservoir modeling results, a decision was made to scale the project to the production capacity of 23A-8 for an initial conservative phase of development. This conservative phased approach was chosen due to the challenge in finding suitable re-injection and also to ensure balancing pressure support to the geothermal reservoir and springs. From the test, it was also determined that additional injection capacity was necessary in order to accommodate 100% re-injection of fluid from 23A-8.

5.2 Ormat Exploration 2017 - 2022

After the long-term test and during 2017, well 24-8 was re-entered with the goal of deepening the well to cross additional ENE-striking faults defined at the range front in the footwall of the DVF in the Nine Hill Tuff unit and indicated by healed fractures encountered shallow in the 23-8 and 23A-8 wells. Drilling activities for 24-8RD commenced on 8/17/2017 until the well was completed directionally to 1463 m (4800 ft) on 9/21/2017. Well 24-8RD was completed with a 9-5/8" liner inside 13-3/8" casing from 637.4 – 1034.5 m (2710 ft to 3394 ft), and a 13" open hole from 1038.1 – 1463 m (3406 to 4800 ft). Basin-fill sediments were encountered to 993.7 m (3260 ft) in contact with Triassic slate and metasiltstone basement rocks below. The metasedimentary formation forms an intrusive contact with granodiorite around 1320 m (4330 ft), and granodiorite persists to the bottom of the hole. Minor fluid losses and drilling breaks were encountered near 1067 m and 1219.2 m (3500 ft and 4000 ft), respectively. An image logged confirmed that two ENE-striking faults were crossed near these depths. However, the rig injection test yield injectivity indices ranging from 1.5 to 1.7 GPM/psi indicating low permeability.

Further injection capacity was still required for the Dixie Meadows project, so in 2019, wells 24-8 and 42-9 were perforated within their respective 13-3/8" casing intervals. Well 24-8RD2 regained permeability (with an injectivity index of 12 GPM/psi) associated with the original feedzones of 24-8 within the basin-fill sediments between approximately 899 – 930 m (2950 to 3050 ft) depths. After perforation, well 42-9 still exhibited low permeability (injectivity index of 0.14 GPM/psi). It was thus deemed necessary to conduct further exploration drilling to find additional permeability suitable to distribute injectate.

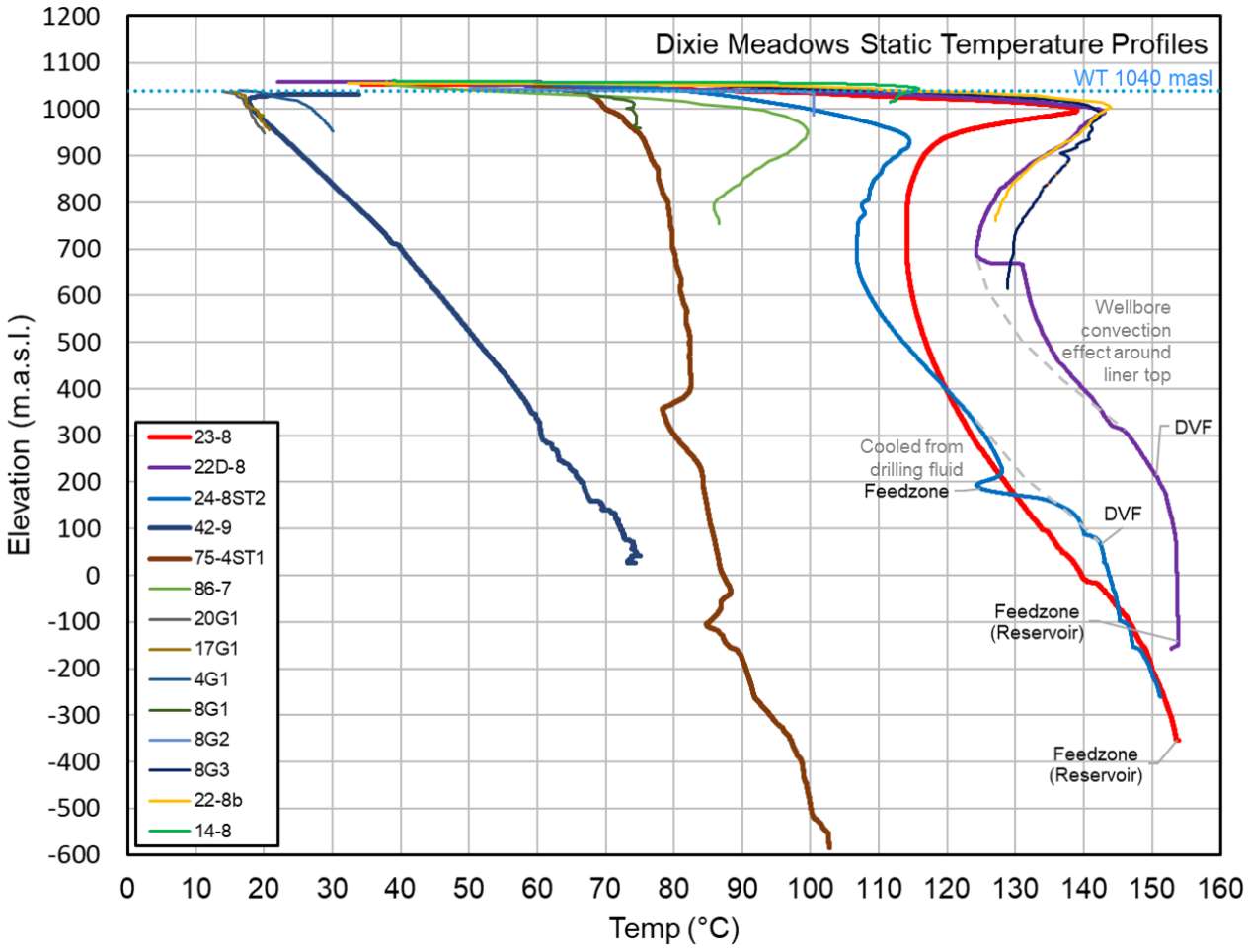

Figure 9: Static temperature profiles from Dixie Meadows. Dashed grey lines represent interpreted static reservoir conditions where logs are affected by cooling or intra-wellbore convection.

Well 22D-8 was drilled adjacent to 22-8b in 2019 and attempted to intersect the ENE-striking production fault at a depth near 675.1 m (2215 ft) and within the basin-fill sediment formation. However, no losses were encountered in 22D-8 near the anticipated depths so the well was deepened vertically to 1227 m (4025 ft) in attempt to explore for additional permeability. The well was drilled through 841.3 m (2760 ft) of basin-fill sediments above Jurassic granodiorite and Triassic slate and metasiltstone formations. The Dixie Valley Fault marks the contact between the basin-fill sediments and older basement rocks at this depth although no fluid losses are associated with the structure. Upon deeper drilling within Triassic slate, the well encountered total loss of circulation at 1208 m (3963 ft), after which the well was completed to 1227 m (4025 ft). The final completion consisted of 8.5" casing to 411.5 m (1350 ft), 6-1/8" hole to 1227 m (4025 ft), and 4.5" slotted liner 409 – 1222.3 m (1342 to 4010 ft). A five-hour injection test provided an injectivity index of 17 GPM/psi for this well. An FMI tool was logged in the hole and open E-W and ENE-striking fractures correspond with the feedzone depths and are similar in orientation and aperture to that encountered in 23A-8. Well 22D-8 was considered a success and a useable injection well; however, because 22D-8 and 23A-8 showed strong pressure communication and their feedzones are separated by <300 m, there was concern for rapid connection to the 23A-8 feedzones. So additional injection was sought to support the expected flow rates from 23A-8.

The geologic model and drilling data were revisited to identify multiple targets which could be intercepted by drilling and increase the likelihood of success. Well 14-8 was selected with the goal of testing ENE-striking faults both within the basin-fill sediments and in Triassic slate formation beneath the DVF. As a contingency plan, the ENE-striking production fault was considered a deeper target near 1676.4 m (5500 ft). Well 14-8 was drilled from 4/9/2020 to 4/19/2020 and completed shallow to a total depth of 163 m (535 ft). While drilling at 143.5 m (471 ft) within basin-fill sediments, total fluid circulation was lost due to the intersection a permeable fault zone. The final construction of the well consists of 13-3/8" casing to 129.5 m (425 ft), 17.5" hole to 163 m (535 ft), and a 9-5/8" slotted liner to 161 m (528 ft). An injection test performed on the well yielded injectivity indices ranging from 10.6 to 21 GPM/psi. The well was deemed a success and provided enough remaining capacity to accommodate the total 4700 GPM of injectate.

The completion of the 14-8 also marked the completion of a successful geothermal wellfield development for Dixie Meadows. In summary the field consists of a single highly permeable production well 23A-8 which is planned to produce 5200 GPM flow of 150°C reservoir fluids. The injection field configuration allows flexibility in which the total 4700 GPM of injectate may be distributed as needed between three injection wells (14-8, 24-8RD2, and 22D-8) into shallow (144 m), intermediate (900 m), and deep (1210 m) feedzones such that pressure support to the geothermal reservoir and springs may be supported. Following the successful wellfield development campaign, the conceptual model of the system was refined, and this information was integrated into a numerical model to test development scenarios. From this work, Ormat designed and procured the manufacturing of a ~15 MWe Gross binary powerplant.

Well	Type	Completion Date	Casing Completion	Hole Diameter	Liner	Lost Circulation	Feedzones	Maximum Temperature (Celcius)	Prod/Inj Index gpm/psi	(PI vs II)
22-8b	Monitor	7/27/2012	4.5" to 274'	HQ 3.895" to 1000'	2-3/8" to 1000'	N/A	N/A	143.9	N/A	
86-7	Monitor	8/9/2012	4.5" to 293'	HQ 3.895" to 1000'	2-3/8" to 1000'	N/A	N/A	101.7	N/A	
23-8	Monitor	10/20/2015	4.5" to 829'	HQ 3.895" to 4700'	2-3/8" to 4692'	4598'	4598 - 4647'	153.3	0.8	II
23A-8	Production	3/2/2016	16" to 2098.5'	14-3/4" to 4758'	9-5/8" to 4733'	4583'	4554 - 4640'	150.6	142.0	PI
24-8RD2	Injection	9/21/2017	13-3/8" to 2813'; 9-5/8" 2710 to 3394'	8.25X13" 3394 to 4800'		2949'; 3149	2949 to 3025'; 3149'; 4002'	151.2	10.0	II
24A-8	Monitor	4/18/2016	4.5" to 151'	HQ 3.895" to 750'	2-3/8" to 750'	N/A	N/A	74.4	0.2	II
42-9	Monitor	10/26/2011	13-3/8" to 3721'	17.5" to 3750' 12-1/4" to 7442'		N/A	N/A	95.9	0.4	II
14-8	Injection	4/19/2020	13-3/8" to 425'	17.5" to 535'	9-5/8" 404 to 528'	471'	471-476'	115.9	13.7	II
22D-8	Injection	8/1/2019	7" to 1340'	6-1/8" to 4025'	4.5" 2407 to 4010'	3963'	3963' to 3988'	153.8	18.0	II
75-4/75-4ML	Monitor	3/25/2017	13-3/8" to 2493'	12-1/4" 2493 to 5000'/ 12-1/4" 2316 to 5476'	N/A/ 9-5/8" 2194 to 4981" & 5" 4912 to 5471'	N/A	3560 to 3900'	96.9	2.7	II
21-9	Monitor	8/1/2011	10" to 100'	8-5/8" to 1000'	6" to 1000'	N/A	N/A	22.9	N/A	

Table 3: Summary of well completions

6. GEOPHYSICS

Geophysical data including airborne magnetics, ground-based gravity, and magnetotellurics (MT) were used to help constrain the conceptual model at Dixie Meadows. These methods help inform depth to basement, define major fault trends, and map out patterns of geothermal alteration.

6.1 Gravity Data

Gravity data were collected in three phases between 2010 and 2016. Measurements were collected on Lacoste and Romberg Model-G gravimeters with a reading resolution of 0.01 milligals. Positioning was obtained using survey grade GPS receivers with centimeter-level accuracy. In total, 1716 gravity stations were recorded. These data were processed using Geosoft software to a complete Bouguer anomaly (CBA). For this paper, a total of 1211 gravity stations were gridded over the area of interest shown in panels A, B, and C of Figure 10. Figure 10A shows the complete Bouguer anomaly using a reduction density of 2.35 g/cm^3 and gridded at 60 m using a minimum curvature routine. The complete Bouguer anomaly was then upward continued by 50 m prior to calculation of the horizontal gradient magnitude (HGM, Figure 10B) and the first vertical derivative (1VD, Figure 10C).

6.2 Airborne Magnetic Data

A high-resolution aeromagnetic survey was commissioned by the USGS in 2002 (Grauch, 2002) for the purposes of geothermal exploration in Dixie Valley. For this project, a part of this survey has been re-gridded over the Dixie Meadows AOI (Figure 10D). The survey was collected on a cesium-vapor magnetometer flown by helicopter at an elevation of 120 m above the land surface with line spacing of 200 m. Flight line azimuth is N30°W, roughly perpendicular to the axis of the Stillwater range.

The total-field magnetic intensity was converted to a magnetic anomaly by removing the International Geomagnetic Reference Field (IGRF), and then gridded at 50 m using a minimum curvature algorithm. A reduction-to-pole transformation (RTP) was then applied to the grid, which migrates magnetic anomalies over their respective sources (Baranov and Naudy, 1964; Blakely, 1995).

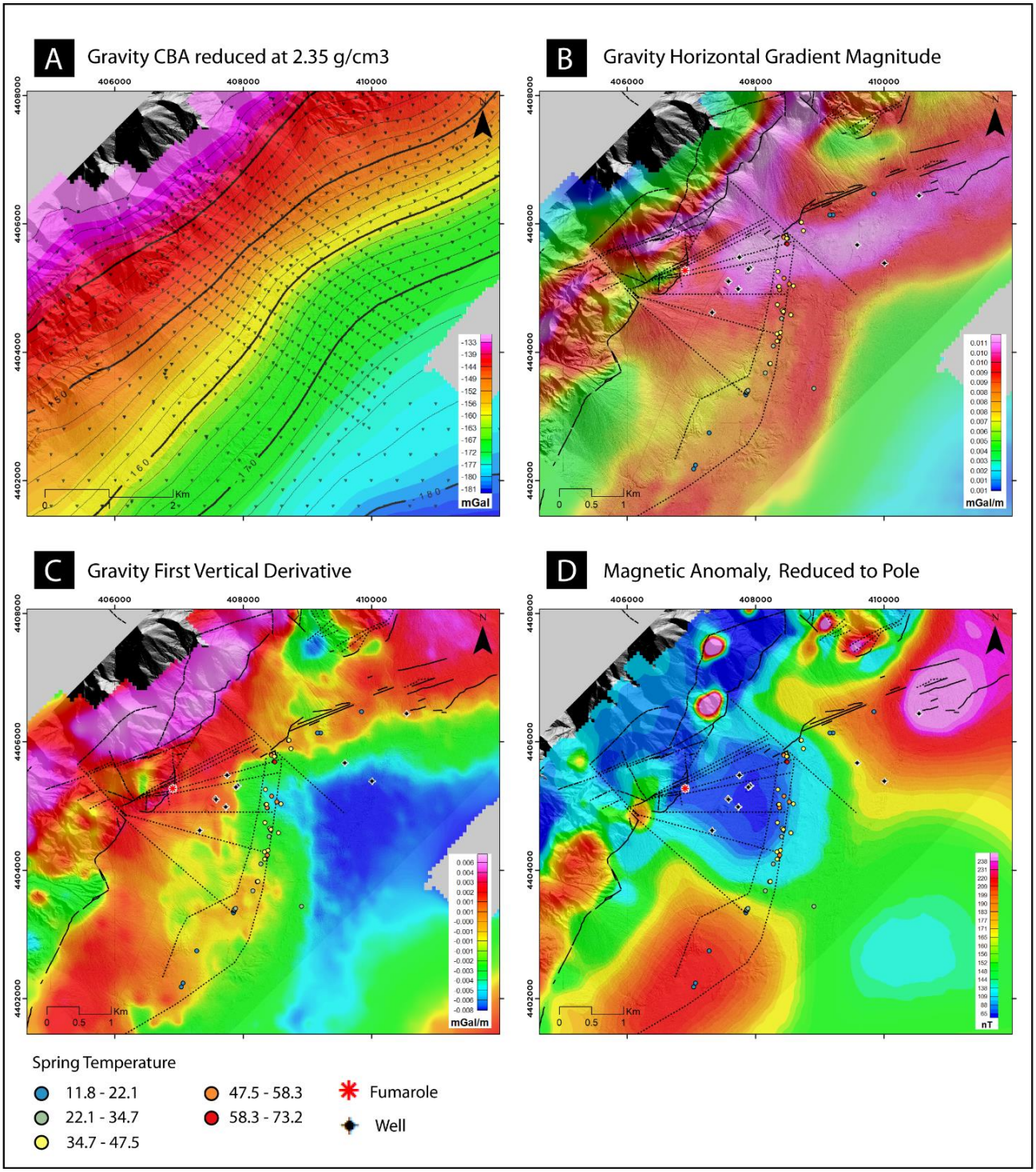

Figure 10: Potential field data over Dixie Meadows. Panels B, C & D contains fault linework (black lines), the location of fumaroles, springs, and well locations. The grid in each panel is made partially transparent to see the hill shade of topography below it. Panel A: Complete Bouguer Anomaly, reduced at 2.35 g/cm^3, gridded at 60 m and contoured at 2 mGal. Gravity stations are shown as gray inverted triangles. Panel B: horizontal gradient magnitude of the 50 m-upward continued CBA. Panel C: First vertical derivative of the 50 m upward continued CBA. Panel D: Reduced-to-pole magnetic anomaly map gridded at 50 m.

6.3 Magnetotelluric Data

Broadband MT data were collected over the Dixie Meadows prospect in four separate phases in 2010, 2011, 2016 and 2018. These stations are shown as inverted triangles in Figure 11A. These datasets were combined for a total of 173 MT stations to produce an inverse 3D resistivity model over the Dixie Meadows prospect.

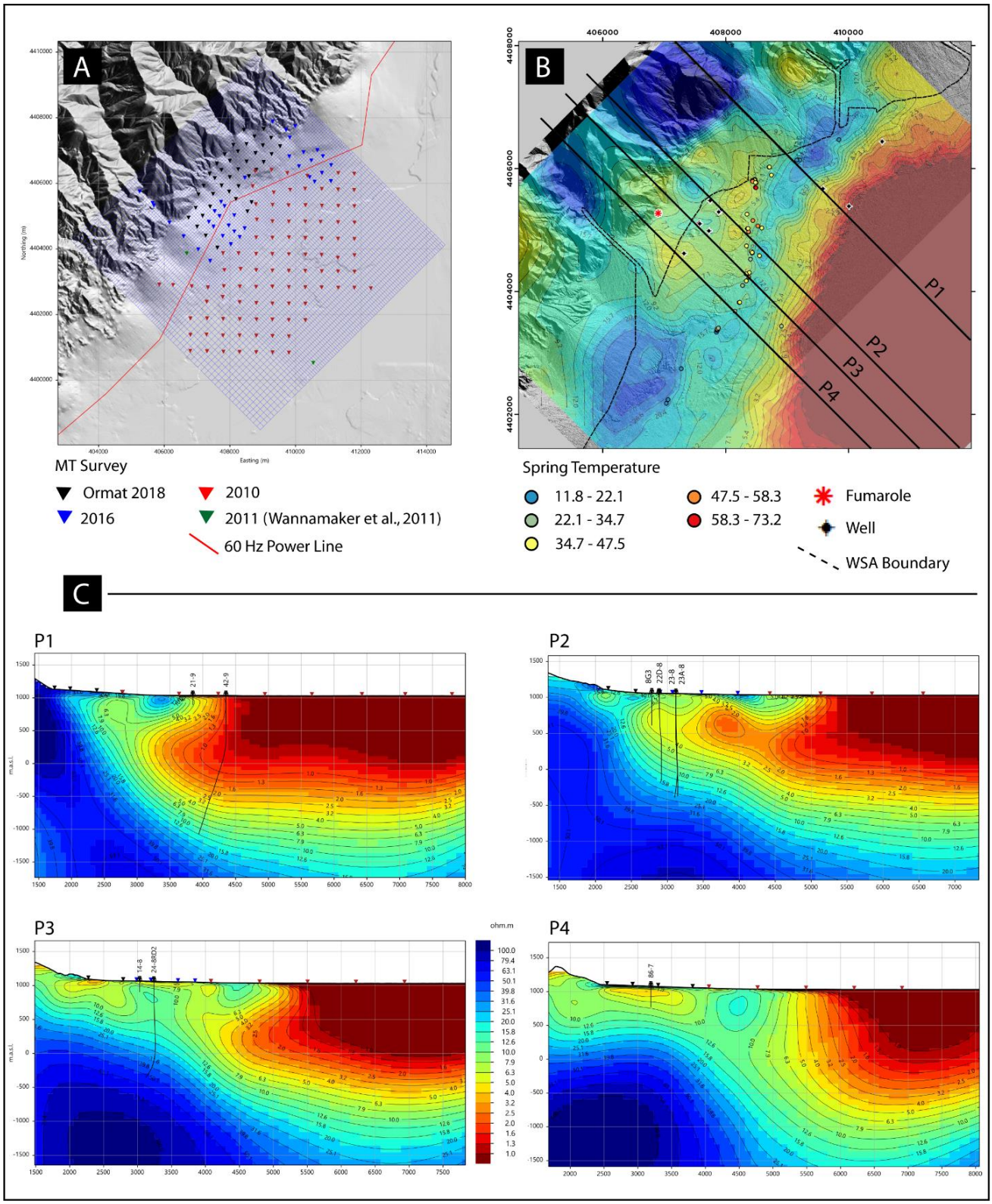

Figure 11: MT station locations, 3D model design and results. Panel A: Model mesh core areas, excluding padding cells (blue grid). MT stations by survey are shown as triangles. Approximate power line location shown as a red line. Panel B: constant elevation 1000 m slice through the 3D model. including springs, fumarole, well locations, WSA boundary, and profile locations. Panel C: Cross -section P1 – P4 through the 3D model, with nearby MT stations and well tracks projected onto each section.

Several stations were negatively impacted by a 60 Hz, 230 kV power line that bisects the survey (Figure 11A, red line). This line transmits power from the 60 MW (net) Dixie Valley Power Plant located to the northeast. Although 60 Hz notch filters and a remote reference station were deployed for each of the above-mentioned surveys, near-field effects from the power line could not be removed in all cases. Near-field noise violates the plane wave assumption inherent in MT data processing. The impacts are easy to identify and remove from the data, however. A sudden increase in the apparent resistivity and decrease in the phase between 16 – 0.8 Hz was found to be typical in these datasets. Data suspected of being influenced by power line noise was not included in modeling routines.

6.4 Magnetotelluric Modeling

Metrics of dimensionality in the observed MT data infer a complex 3D structure, which necessitates the use of a 3D modeling routine. The combined tensor data of 173 stations were rotated by 45 degrees CW to align with a 3D model mesh and were then edited to remove spurious points and the impacts of power line noise. Tipper data was included in the modeling routine from the 2010 and 2011 datasets. A total of 32 frequencies per decade were modeled after decimating the data to 5 points/decade, covering a range of 0.002512 – 3981 Hz. No effort was made to correct for static distortions in the data (frequency-independent deflections of the apparent resistivity curves) since they can contain useful information when topography is accounted for and the data are modeled in 3D (Soyer et al., 2018).

The data were modelled using the RLM-3D nonlinear conjugate gradient inversion code (Rodi and Mackie, 2001). This routine employs a minimum structure Tikhonov approach (Tikhonov and Arsenin, 1977) where an objective function that contains a smoothing term is iteratively minimized. A model mesh was generated with an inner core area of 75 m x 75 m and an outer core area of 150 m x 150 m (Figure 11A, blue grid). Topography was included in the model and discretized in 5m increments. Padding cells extended in the x, y, and z directions for > 50 km, for a total of 2.29 million cells. A homogeneous starting model value of 3 Ωm was assigned. Earlier inverse models in the workflow helped identify issues with the input data and explore the impact of various inversion parameters on the model space. A final model suite used a 5% error floor on the components of Z and 0.02 on the tipper. After running for 50 iterations, the model was re-started using a lower vertical regularization setting (0.01 from 0.03). The final model ran for an additional 35 iterations and achieved an RMS error of 1.23.

The 3D MT model is shown in panels B and C of Figure 11. Panel B shows a shallow constant elevation slice at 1000 m above sea level. For reference, the elevation of the valley floor is ~ 1030 m, and the springs discharge at ~1040 m. Panel C shows cross-sections P1 – P4 through the model with well paths projected onto the section (black lines).

6.5 Geophysical Interpretations

6.5.1 Gravity

The HGM (Figure 10B) shows several trends where major contrasts in density are apparent. Along the range front, a high gradient is observed where the DVF juxtaposes dense Triassic slate and siltstone (TRs) to alluvial fan deposits. This high gradient deviates from the DVF where it instead juxtaposes Tertiary tuffs from the alluvial fans, implying that the tuffs have appreciably lower densities than the older units. The most prominent trend in the HGM data is an ENE trend that terminates near the steam vents. This gradient is likely caused by basin-bounding faults, offsetting alluvium against denser units. Given the numerous observations of ENE striking fractures from the well data, it is likely that this gradient represents a set of sub-parallel structures. A lesser lineament follows the interface of the alluvial fans with finer and lower density valley fill material. This gradient lines up with a sharp transition to lower near-surface resistivity values seen in the 3D MT model (Figure 10B).

The first vertical derivative of the gravity data (Figure 10C) also suggests that the Tertiary tuffs are lower in density than the Triassic units. Cooler colors along the range front correlate well with the tuffs, and a sharp change to high gradients (warm colors) is observed where Triassic slate makes fault contact with the alluvial fans north of the wells. Notably lacking in the gravity data is any evidence for shallow densification caused by geothermal processes. Given the evidence for geothermal outflow and alteration mineralization, it is curious that a body of massive opalized silica is not apparent. Massive silica can form near the water table in the presence of geothermal outflow. Such observations have been noted in other low-enthalpy systems in the Basin and Range such as San Emidio (Folsom et al., 2020), and at Don A. Campbell (unpublished report). Patterns of vertically zoned alteration near the water table are well described in the literature (Sillitoe, 1993; Hedenquist, 2000; Simmons et al., 2005 and others). Extensive chalcedony beds are not abundantly obvious in the shallow well data, either. Wells that encounter shallow permeability (E.g., 14-8) do so in the presence of calcite alteration instead. One potential cause for this is mixing of cooler groundwaters with the geothermal outflow, which may prevent super-saturation of silica. The presence of both hot and cool springs nearby and the relatively low silica values from sampled hot springs supports this theory.

6.5.2 Magnetics

In contrast to the gravity interpretation, evidence of near-surface alteration is apparent in the magnetic data (Figure 10D). A significant magnetic low is observed over the Dixie Meadows geothermal system, bound by the steam vents to the west and the springs to the east. Although the wavelength of this feature implies a deeper source, we conclude that the demagnetization occurs within the upper 10's of meters. The proposed mechanism is the destruction of magnetite caused by alteration/sulfidation below the boiling watertable along the shallow outflow path and also from acid sulfate alteration in the vadose zone closer the range front where there is evidence of native sulfur accumulating near the steam vents. This magnetic low correlates well with the shallow low-resistivity anomaly seen in the constant-elevation slice though the 3D MT resistivity model (Compare Figure 11D with Figure 10B).

There are several descriptions in the literature of low magnetic intensities observed over high enthalpy geothermal systems (Anderson et al., 1987; Hochstein et al., 1997; Soengkono, 2016). Direct measurements of magnetic susceptibility from core samples at the Wairakei field in New Zealand confirm the most intense demagnetization occurs at ~500 m deep (Allis, 1990), slightly above the producing reservoir. The proposed mechanism for this destruction is a two-phase zone where CO_2 rich gases recondense and form

secondary acidic fluids. In this zone magnetite is destroyed or replaced by minerals such as pyrite. Processes like this are less likely to occur in the non-magmatic, low enthalpy systems of the Basin and Range. Nevertheless, magnetic lows are periodically observed in their vicinity. Only a few fields in Nevada have magnetic lows directly overtop of proven reservoirs. These include Dixie Meadows and Don A. Campbell (unpublished report). At each of these fields, however, the case can be made for shallower sources of demagnetization. Many other greenfield prospects exhibit magnetic lows, although a general lack of drilling data does not provide a conclusive answer as to why.

The magnetic data also exhibits sharply lower values over the range near units TRs, Jb and Jg2. We interpret these lows as being caused by reverse-remanent magnetism. The alluvial fans are mostly composed of detritus from these rocks and from the younger tuffs. We infer that they have lost any component of remanent magnetism due to their sedimentary nature (are no longer in-situ) and are only magnetized by their remaining magnetic susceptibilities. Such units may be easily demagnetized in the presence of near-boiling geothermal outflow.

6.5.3 Magnetotellurics

In plan view, shallow conductive anomalies (< 5 Ωm) are found to overlie the known geothermal reservoir. These features are easily seen in a depth slice through the resistivity volume at 1000 m elevation (Figure 11B). These anomalies encompass the production and injection wells, meet the steam vents on the west, and truncate up against the springs to the east. This zone correlates well with the magnetic low seen in Figure 11D. Note that the 1000 m elevation slice is the same elevation where peak shallow temperatures are observed in the wells (Figure 9). We interpret these shallow conductive anomalies as being caused by advanced argillic alteration of the fan material to clays. Swelling clay alteration products (montmorillonites) with high cation exchange capacity have notably low resistivities (Ussher et al., 2000). Generally, these values can approach 1 Ωm but rarely go below it. Exceptionally low resistivity values are observed over the valley floor at Dixie Meadows and are seen in each cross-section of Figure 11. Apparent resistivity values from the most basin-ward MT sites are ~0.2 Ωm at higher frequencies. These conductive anomalies are not geothermal in origin but are instead attributed to salt-bearing playa deposits. To the east of the springs and in the presence of these very conductive sediments, shallow geothermal outflow correlates with a more resistive zone (Figure 12). The reason for this is not well understood but may be caused by the flushing away of high TDS playa fluids with fresher geothermal outflow and cooler spring waters. Alternatively, this resistive zone may be caused by its sedimentary origins.

At greater depths the MT model helps inform the depth of basin fill and generally predicts the depth and the dip of the DVF. We find that the 13-15 Ωm contours tend to agree with the depth of alluvium underneath the fans.

7. INTEGRATED CONCEPTUAL MODEL

Geothermal upflow at the Dixie Meadows geothermal field is localized along a set of dilated fractures associated with steeply-dipping ENE-striking faults. Favorable dilation (below Coulomb failure) is facilitated by local rotation and enhancement of the stress field near a bend in the Dixie Valley Fault. The system is hosted in fractured Paleozoic metasediments and Mesozoic intrusive rocks, with fracture apertures reaching up to 12", enabling the high permeability encountered by 23A-8 (142 GPM/psi). The reservoir chemistry is consistent with a non-magmatic system hosted in Cl-deficient host rocks (i.e., a low leachable volume of volcanic glass) and has a correspondingly low TDS (850-1030 ppm) and low NCG concentration (~0.1 wt%).

140°C outflow is channeled in an east and southeast direction along permeable strata in the upper 150 m of the surface and discharges as hot and warm springs at the toe of the alluvial fan where the water table (~1040 masl) intersects the surface. Eastward migration of this subsurface outflow fluid is limited by the occurrence of low permeability playa deposits that interfinger with alluvial sediments east of the springs. The hottest grouping of these springs (~70°C) occur near and 300 m SE of the inferred trace of the ENE production fault. The outflow characteristics at Dixie Meadows is corroborated by drilling data that evidences shallow thermal fluids moving laterally within semi-permeable sand-gravel horizons, sourced from the rangefront to the NW within the Wilderness Study Area (WSA, Figure 1). The chemistry of these springs indicates dilution with groundwater, which is expected to be sourced from the Stillwater range, directly to the west. There are also weak steam vents that occur near the intersection of the ENE Production Fault with the DVF. Hydrothermal alteration of alluvial clasts along this outflow create a pronounced demagnetized zone that reaches from the range front to the springs at the edge of the alluvial fan.

Artesian pressures, a phenomenon that is common to some deep circulation geothermal systems, are not encountered in the Dixie Meadows reservoir. The lack of artesian pressures at Dixie Meadows may be related to the observations of pronounced channelized shallow outflow and widespread surface manifestations, which essentially reflect a notable hydraulic release through any local aquitard units that may exist. The active seismicity of the DVF, which had a M 6.8 event near Dixie Meadows in 1954, may play a role in enabling notable fluid release to the shallow subsurface and surface, and the resulting lack of artesian pressures in the reservoir.

Elements of the conceptual model outlined above provided a framework to the numerical model in which reservoir parameter sensitivities and development scenarios were tested. Evaluation of these sensitivities helped determine the size and suitable configuration of a wellfield development to support a phased development, with the first phase being a 15 MW gross development at Dixie Meadows.

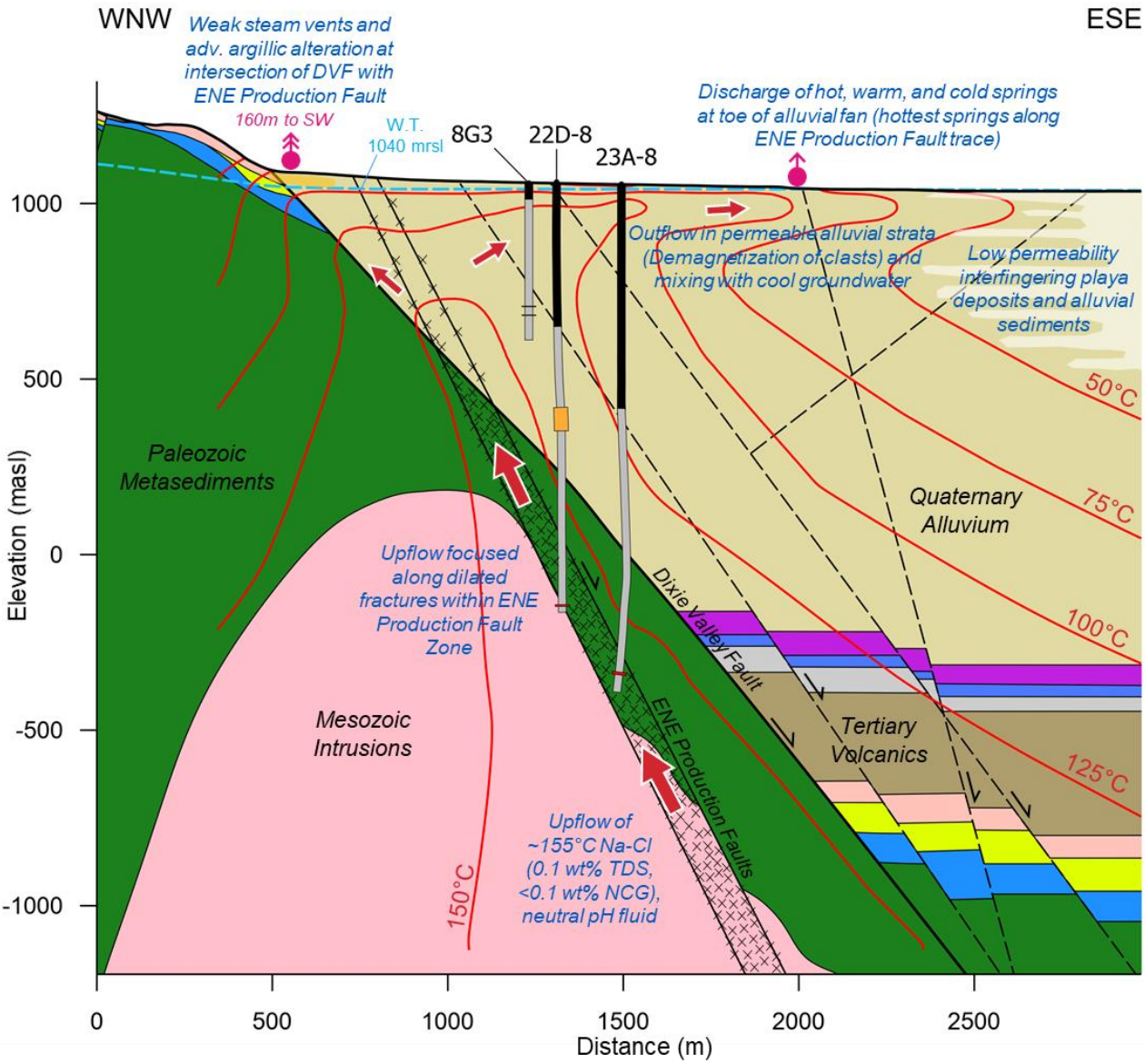

Figure 13: Conceptual model cross-section showing geology (above) and 3D MT inversion model (below).

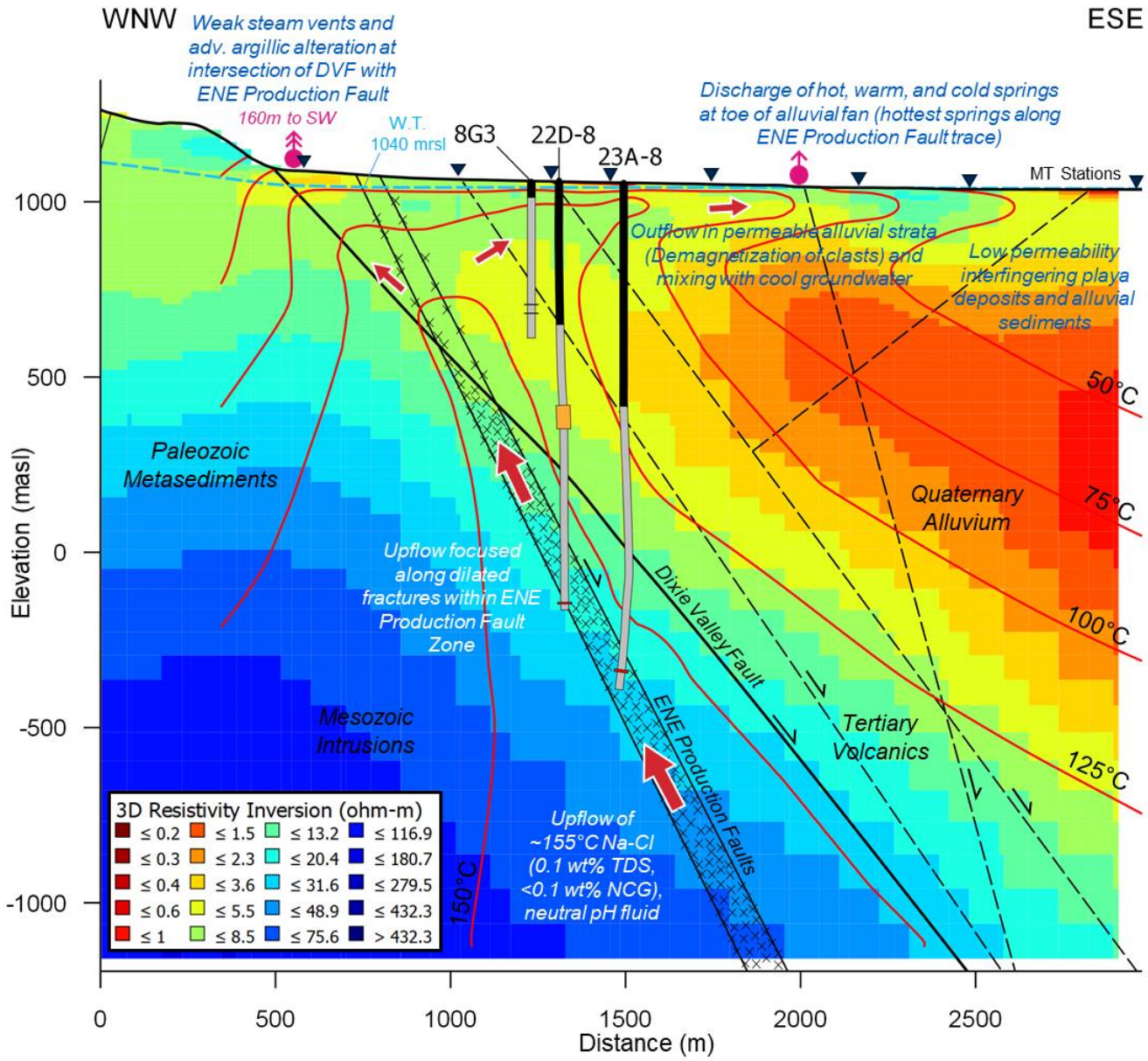

8. CONCLUSIONS

Early geothermal exploration efforts at Dixie Meadows beginning in the 1970s were unsuccessful at understanding the geometry and structural controls of the reservoir or making a resource discovery. The exploration campaign deployed by Ormat at Dixie Meadows culminated in an updated conceptual model that ultimately was used to make a resource discovery and achieve a successful wellfield development program. The multidisciplinary approach to the interpretation of geoscientific and reservoir data was integral to the refinement of the conceptual and numerical models for Dixie Meadows, and to the well targeting successes.

9. ACKNOWLEDGEMENTS

The authors would like to thank Ormat for the opportunity to publish this paper. We would also like to acknowledge all those who worked and made significant contributions to the Dixie Meadows project including: Paul Schwering for his thesis work and discovery of the 8G3 abandoned wellhead; Christopher Henry for facilitating radiometric age dating; Elton Colbert and Eddie Lay for organizing and overseeing the long-term test; Doug Perkin for conducting the MT survey; and Zvi Krieger for managing the exploration efforts, which ultimately led to a successful wellfield development.

REFERENCES

Akerley, J., Batzli, S., Cardiff, M. A., Walsh, P., & Feigl, K. L. (2018). Analysis of a Long-Term Test by Inverse Modeling Surface Deformation as Measured by InSAR. *43rd Workshop on Geothermal Reservoir Engineering, Stanford University*.

Allis, R. G. (1990). Geophysical anomalies over epithermal systems. *Journal of Geochemical Exploration*, *36*(1-3), 339-374.

Bell, J. W., & Katzer, T. (1987). *Surficial Geology, Hydrology, and Late Quaternary Tectonics of the IXL Canyon Area, Nevada: As Related to the 1954 Dixie Valley Earthquake* (Vol. 102). Nevada Bureau of Mines & Geology, University of Nevada-Reno.

Blakely, R. J. (1996). *Potential theory in gravity and magnetic applications*. Cambridge university press.

BLM. (2021). Environmental Assessment ORNI 32, LLC Dixie Meadows Geothermal Utilization Project.

DOI-BLM-NV-C010-2016-0014-EA. 260p.

Booker, J. R. (2014). The magnetotelluric phase tensor: a critical review. *Surveys in Geophysics*, *35*(1), 7-40.

Burke, D. B., & McKEE, E. H. (1979). Mid-Cenozoic volcano-tectonic troughs in central Nevada. *Geological Society of America Bulletin*, *90*(2), 181-184.

Caldwell, T. G., Bibby, H. M., & Brown, C. (2004). The magnetotelluric phase tensor. *Geophysical Journal International*, *158*(2), 457-469

Caskey, S. J., Wesnousky, S. G., Zhang, P., & Slemmons, D. B. (1996). Surface faulting of the 1954 Fairview Peak (MS 7.2) and Dixie Valley (MS 6.8) earthquakes, central Nevada. *Bulletin of the Seismological Society of America*, *86*(3), 761-787.

Caskey, S. J., Bell, J. W., Ramelli, A. R., & Wesnousky, S. G. (2004). Historic surface faulting and paleoseismicity in the area of the 1954 Rainbow Mountain-Stillwater earthquake sequence, central Nevada. *Bulletin of the Seismological Society of America*, *94*(4), 1255-1275.

Delwiche, B. (2011) Geologic Map of Dixie Meadows in Dixie Valley, Churchill County, NV., 1:3000, unpublished work.

Dowdle, W. L., & Cobb, W. M. (1975). Static formation temperature from well logs-an empirical method. *Journal of Petroleum Technology*, *27*(11), 1326-1330.

Folsom, M., Libbey, R., Feucht, D., Warren, I., & Garanzini, S. (2020). Geophysical Observations and Integrated Conceptual Models of the San Emidio Geothermal Field, Nevada. In *Proceedings of the 45th Workshop on Geothermal Reservoir Engineering, Stanford University, Stanford, CA, USA 21p*.

Grauch, V. J. S. (2002). *High-resolution aeromagnetic survey to image shallow faults, Dixie Valley geothermal field, Nevada* (pp. 1-13). US Department of the Interior, US Geological Survey.

Hedenquist, J. W., Arribas, A., & Gonzalez-Urien, E. (2000). Exploration for epithermal gold deposits.

Henry, C.D., Faulds, J.E., dePolo, C.M., Davis, D.A. (2004a). Geology of the Dogskin Mountain Quadrangle, Washoe County, Nevada: Nevada Bureau of Mines and Geology Map 148, scale 1:24,000, 13 p. Hammond, W. C., & Thatcher, W. (2004). Contemporary tectonic deformation of the Basin and Range province, western United States: 10 years of observation with the Global Positioning System. *Journal of Geophysical Research: Solid Earth*, *109*(B8).

Hickman, S. H., Zoback, M. D., Barton, C. A., Benoit, R., Svitek, J., & Summers, R. (1999). *Stress and permeability heterogeneity within the Dixie Valley geothermal reservoir: Recent results from well 82-5* (No. DOE/ID/13762). USDOE Idaho Operations Office, Idaho Falls, ID; Oxbow Geothermal Corporation (US).

Hochstein, M. P., & Soengkono, S. (1997). Magnetic anomalies associated with high temperature reservoirs in the Taupo Volcanic Zone (New Zealand). *Geothermics*, *26*(1), 1-24.

Huang, S., Xia, K., & Dai, F. (2012). Establishment of a dynamic Mohr–Coulomb failure criterion for rocks. *International Journal of Nonlinear Sciences and Numerical Simulation*, *13*(1), 55-60.

Iovenitti, J., Sainsbury, J., Tibuleac, I., Karlin, R., Wannamaker, P., Maris, V., ... & Swyer, M. (2013, February). EGS exploration methodology project using the Dixie Valley geothermal system, Nevada, status update. In *Proceedings 38th Workshop on Geothermal Reservoir Engineering Stanford University, Stanford, California, February* (pp. 11-13).

Kreemer, C., Hammond, W. C., Blewitt, G., Holland, A. A., & Bennett, R. A. (2012, April). A geodetic strain rate model for the Pacific-North American plate boundary, western United States. In *EGU General Assembly Conference Abstracts* (p. 6785).

LaFehr, T. R. (1991). An exact solution for the gravity curvature (Bullard B) correction. *Geophysics*, *56*(8), 1179-1184.

Littlefield, E. (2011), Raster Classifications of Mineral Assemblages using Hyperspectral Data at Dixie Meadows. [unpublished maps]

Nimz, G., Janik, C., Goff, F., Dunlap, C., Huebner, M., Counce, D., & Johnson, S. D. (1999). Regional hydrology of the Dixie Valley geothermal field, Nevada: preliminary interpretations of chemical and isotopic data.

Nosker, S. A. (1981). *Stratigraphy and structure of the Sou Hills, Pershing County, Nevada* (Doctoral dissertation, University of Nevada, Reno).

Oldow, J. S. (1984). Evolution of a late Mesozoic back-arc fold and thrust belt, northwestern Great Basin, USA. *Tectonophysics*, *102*(1-4), 245-274.

Page, B.M. (1965). Preliminary geologic map of a part of the Stillwater Range, Churchill County, Nevada, Nevada Bureau of Mines

Parker, R. L., & Booker, J. R. (1996). Optimal one-dimensional inversion and bounding of magnetotelluric apparent resistivity and phase measurements. *Physics of the Earth and Planetary Interiors*, *98*(3-4), 269-282.

Riehle, J. R., McKEE, E. H., & Speed, R. C. (1972). Tertiary volcanic center, west-central Nevada. *Geological Society of America Bulletin*, *83*(5), 1383-1396.

Rodi, W., & Mackie, R. L. (2001). Nonlinear conjugate gradients algorithm for 2-D magnetotelluric inversion. *Geophysics*, *66*(1), 174-187.

Sillitoe, R. H. (1997). Epithermal models: genetic types, geothermal controls and shallow features. *Mineral Deposit Modeling*.

Simmons, S. F., White, N. C., & John, D. A. (2005). Geological characteristics of epithermal precious and base metal deposits.

Slemmons, D. B. (1957). Geological effects of the Dixie valley-Fairview peak, Nevada, earthquakes of December 16, 1954. *Bulletin of the Seismological Society of America*, *47*(4), 353-375.

Soengkono, S. (2016). Airborne magnetic surveys to investigate high temperature geothermal reservoirs. In *Advances in Geothermal Energy* (p. 113). IntechOpen.

Soyer, W., Mackie, R., & Miorelli, F. (2018, June). Optimizing the estimation of distortion parameters in magnetotelluric 3D inversion. In *80th EAGE Conference and Exhibition 2018* (Vol. 2018, No. 1, pp. 1-5). European Association of Geoscientists & Engineers.

Speed, R.C. (1976). Geologic Map of the Humboldt Lopolith, scale 1:81050, *GSA Map Chart Series*, MC-14.

Tikhonov, A. N., & Arsenin, V. I. (1977). *Solutions of Ill-posed Problems: Andrey N. Tikhonov and Vasiliy Y. Arsenin. Translation Editor Fritz John*. Wiley.

Ussher, G., Harvey, C., Johnstone, R., & Anderson, E. (2000, May). Understanding the resistivities observed in geothermal systems. In *proceedings world geothermal congress* (pp. 1915-1920). Japan: Kyushu.

Vikre, P. G. (1994). Gold mineralization and fault evolution at the Dixie Comstock Mine, Churchill County, Nevada. *Economic Geology*, *89*(4), 707-719.

Wannamaker, P. E., Maris, V., Sainsbury, J., & Iovenitti, J. (2013, February). Intersecting fault trends and crustal-scale fluid pathways below the Dixie Valley geothermal area, Nevada, inferred from 3D magnetotelluric surveying. In *Proceedings of the Thirty-Eighth Workshop on Geothermal Reservoir Engineering, California, USA Stanford University*.

Wesnousky, S., Caskey, S. J., & Bell, J. W. (2003). *Recency of Faulting and Neotechtonic Framework in the Dixie Valley Geothermal Field and Other Geothermal Fields of the Basin and Range* (No. DOE/ID/13620). University of Nevada, Reno (US).